

# Visual Grasping for a Lightweight Aerial Manipulator Based on NSGA-II and Kinematic Compensation

Linxu Fang, Haoyao Chen, Yunjiang Lou, Yanjie Li, and Yunhui Liu

**Abstract**— The grasping control of an aerial manipulator in practical environments is challenging due to its complex kinematics/dynamics and motion constraints. This paper introduces a lightweight aerial manipulator, which is combined with an X8 coaxial octocopter and a 4-DoF manipulator. To address the grasping control problem, we develop an efficient scheme containing trajectory generation, visual trajectory tracking, and kinematic compensation. The NSGA-II method is utilized to implement the multiobjective optimization for trajectory planning. Motion constraints and collision avoidance are also considered in the optimization. A kinematic compensation-based visual trajectory tracking is introduced to address the coupled nature between manipulator and UAV body. No dynamic parameter calibration is needed. Finally, several experiments are performed to verify the stability and feasibility of the proposed approach.

## I. INTRODUCTION

Unmanned aerial vehicle (UAV) equipped with manipulators is a popular research topic due to its considerable potential for various applications [1]-[3], including express transportation, high-altitude construction and maintenance, and operations, which are highly dangerous or unreachable for a human. Although the automatic control of UAV system has been well studied in the literature, it is challenging for those systems with manipulators, mainly due to the largely complex kinematics and dynamics caused by the attached movable manipulator. The contact force uncertainty between the end effector and the operating targets is also an issue for effective control.

Many researchers have already developed several interesting approaches for the design and autonomous control of aerial manipulator systems [4]-[6]. Various task-adaptive grippers for UAV systems have been proposed in the literature. Pounds et al. [1] equipped a helicopter with a manipulator to grasp a block on the ground. Doyle et al. [4] presented a prototype with an avian-inspired passive perching mechanism. Ghadiok et al. [7] designed a special gripper and successfully utilized onboard sensors to locate and grasp an object autonomously.

To realize an autonomous interaction with the complex environmental objects using flexible manipulators is challenging. Some works [8]-[10] for controlling an aerial manipulator were performed; these works include visual

servoing aerial grasping [5][6], nonlinear dynamic control [9], and a predictive control method [10]. Thomas et al. [5] considered an aerial manipulator system equipped with a monocular camera; a nonlinear visual servoing controller for trajectory tracking in the image space was developed. Mebarki et al. [6] proposed an image-based visual servoing scheme by considering the full cross-coupled dynamics and presented a nonlinear integral back-stepping controller to ensure low-level servoing. Garimella et al. [9] presented a nonlinear model-predictive control methodology based on the multibody system dynamics and achieved an optimized performance; however, the optimal control algorithm cannot achieve real-time performance. Kim et al. [10] designed a passivity-based adaptive controller for the combined aerial manipulation system based on the system dynamics and suggested a guidance law utilizing visual information.

An accurate control of an aerial manipulator requires precise modeling of dynamics; nevertheless, dynamics modeling is challenging because many physical parameters, such as rotational inertia [11], are difficult to measure. Most of the relevant works are based on simulations, or they do not consider collision avoidance during grasping. The existing visual servoing approaches are difficult to apply in solving complex collision-free grasping tasks. This paper utilizes a lightweight manipulator to address the dynamic interference problem and proposes a cheap but effective kinematic way to realize automatic object grasping without the need for calibration of dynamic parameters. In this paper, we also aim to develop a scheme for autonomous target tracking, trajectory generation without collision, and vision-based trajectory tracking. The multiobjective optimization method NSGA-II [12] is utilized for trajectory generation. A good performance can be achieved by considering visual feedback compensation, although the target or UAV body is slightly unstable.

## II. PROBLEM FORMULATION

This paper aims to develop a lightweight aerial manipulator system for autonomous target grasping. As shown in Fig. 1, the aerial manipulator consists of a 4-DoF lightweight manipulator and an X8 coaxial octocopter. Fig. 1(b) illustrates the 3D CAD model of the proposed 4-DoF aerial manipulator. Inspired by the design [13], the lightweight aerial manipulator is designed by arranging the power driven units (motor) to the manipulator base to reduce the dynamics instability of the system during manipulator movement. Different from the design in [13], we propose a visual system with a monocular camera and a 1-DoF pitch servo motor to track the target object and control the grasping. The camera rotates in pitch direction driven by the servo motor. Thus, the pitch DoF can maintain the target in the camera's field of view during flying. The manipulator links

\*This work was partially supported by a grant from the National Natural Science Foundation of China (Reference Nos. 61673131 and U1713206) and the Shenzhen Science and Innovation Committee (Reference No. JCYJ20160427183958817).

L.X. Fang, H. Chen, Y.J. Lou, and Y.J. Li are affiliated with the School of Mechanical Engineering and Automation in Harbin Institute of Technology Shenzhen and the State Key Laboratory of Robotics and System, China (hychen5@hit.edu.cn).

Y.H. Liu is affiliated with the Department of Mechanical and Automation Engineering in Chinese University of Hong Kong, Hong Kong, P. R. China. (yhliu@mae.cuhk.edu.hk).

are made of light plastic material through 3D printing. The weight and strength are also verified in the experiments. The developed X8 coaxial octocopter provides sufficient payload for the manipulator and grasped load.

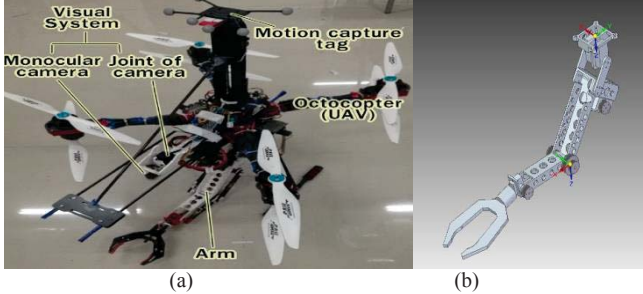


Figure 1. (a) Proposed aerial manipulator. (b) Manipulator's 3D CAD model.

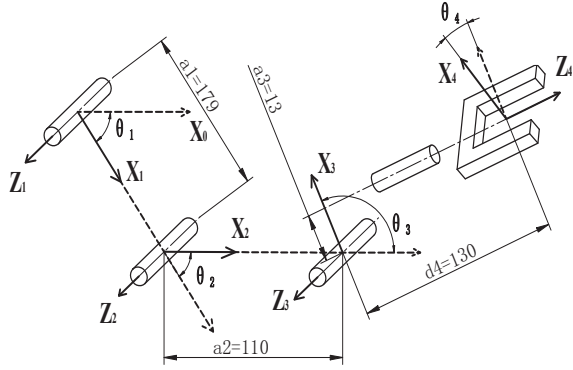


Figure 2. Coordinate frames of the proposed manipulator.

The 4-DoF octocopter and 4-DoF manipulator together provide 8-DoF motion ability and achieve the 6-DoF movement of the end effector. Additional DoFs for internal movement to avoid collision can also be provided. However, controlling the complex system is challenging because the DoFs are coupled. The manipulator motion also affects the octocopter's hovering stability. Dynamic parameters are difficult to calibrate in practical applications, and they also suffer from variation. These problems prevent the aerial manipulator from successfully grasping an object in practical environments. In addition, the implementation of a practical task with the aerial manipulator should satisfy several constraints, e.g., joint limits, collision avoidance, UAV velocity, and joint angular velocity. The end-effector movement distance and time duration should be small to save energy. Generally, all these constraints and objectives cannot be satisfied. Therefore, to implement the autonomous grasping task successfully, a trajectory based on a multiobjective optimization should be generated. This trajectory balances the mentioned constraints and objectives. Furthermore, the trajectory should be corrected in real time due to the disturbance from the UAV body. The manipulator performs the target grasping along the compensated trajectory.

### III. KINEMATICS MODELING

#### A. Kinematics Modeling

Fig. 2 illustrates the relationship between the joints' coordinate frames of the proposed 4-DoF manipulator. The DH parameters are obtained through DH calibration [14]. The transformation of the end effector w.r.t. the first joint base ( $\mathbf{T}_e^0$ ) is given by the following:

$$\mathbf{T}_e^0 = \mathbf{T}_1^0 \mathbf{T}_2^1 \mathbf{T}_3^2 \mathbf{T}_e^3 = \begin{bmatrix} \mathbf{R}_e^0 & \mathbf{t}_e^0 \\ \mathbf{0}_3^T & 1 \end{bmatrix}, \quad (1)$$

$$\text{where } \mathbf{R}_e^0 = \begin{bmatrix} c_{123}c_4 & -c_{123}s_4 & s_{123} \\ s_{123}c_4 & -s_{123}s_4 & -c_{123} \\ s_4 & c_4 & 0 \end{bmatrix},$$

$$\mathbf{t}_e^0 = \begin{bmatrix} a_2c_{12} + a_1c_1 + a_3c_{123} + d_4s_{123} \\ a_2s_{12} + a_1s_1 + a_3s_{123} - d_4c_{123} \\ 0 \end{bmatrix} \quad (2)$$

and  $\mathbf{0}_3 \in \mathbb{R}^3$  denotes zero vector. In this paper, the matrix  $\mathbf{R}_k^i \in \mathbb{R}^{3 \times 3}$  denotes the rotation transformation of frame  $k$  w.r.t. frame  $i$ , and the vector  $\mathbf{t}_k^i \in \mathbb{R}^3$  denotes the translation of frame  $k$  from frame  $i$ . With the combination of the rotation and translation,  $\mathbf{T}_k^i \in SE(3)$  denotes the transformation of frame  $k$  w.r.t frame  $i$ . Moreover, 0 is the manipulator's base frame,  $e$  is the end-effector frame, and the other index  $i \in (1, 2, 3, 4)$  is the link frame number.  $\mathbf{T}_0^b$  is the offset matrix from UAV body frame  $b$  to the manipulator's base frame 0.  $s_4$  and  $c_4$  are the abbreviations of  $\sin \theta_4$  and  $\cos \theta_4$ ,  $s_{12}$  and  $c_{12}$  are the abbreviations of  $\sin(\theta_1 + \theta_2)$  and  $\cos(\theta_1 + \theta_2)$ , and  $s_{123}$  and  $c_{123}$  are the abbreviation of  $\sin(\theta_1 + \theta_2 + \theta_3)$  and  $\cos(\theta_1 + \theta_2 + \theta_3)$ , respectively.

The manipulator's forward kinematics  $\mathbf{T}_e^b$  is as follows:

$$\mathbf{T}_e^b = \mathbf{T}_0^b \mathbf{T}_e^0. \quad (3)$$

The inverse kinematics needs to calculate all the joint angles  $\theta_i (i = 1, 2, 3, 4)$  from the a priori known  $\mathbf{T}_e^0$ . The matrix  $\mathbf{T}_e^0$  can be rewritten as follows:

$$\mathbf{T}_e^0 = \begin{bmatrix} n_x & o_x & a_x & p_x \\ n_y & o_y & a_y & p_y \\ n_z & o_z & a_z & p_z \\ 0 & 0 & 0 & 1 \end{bmatrix}. \quad (4)$$

In addition,

$$\begin{cases} \theta_4 = \tan^{-1}(n_z/o_z) \\ \theta_1 + \theta_2 + \theta_3 = \tan^{-1}(-a_z/a_y) \end{cases} \quad (5)$$

and  $p_z = 0$  because the arm joints are constrained in a planar phase. When the following variables are defined,

$$\begin{cases} k_1 = a_3c_{123} + d_4s_{123} \\ k_2 = a_3s_{123} - d_4c_{123} \\ k_3 = p_x - k_1 \\ k_4 = p_y - k_2 \end{cases}, \quad \begin{cases} s_1 = k_3^2 + k_4^2 - a_1^2 + 2a_1a_2 - a_2^2 \\ s_2 = -(k_3^2 + k_4^2) + a_1^2 + 2a_1a_2 + a_2^2 \\ s = \sqrt{s_1 \times s_2} \\ e_1 = k_3^2 + k_4^2 + a_1^2 + 2a_1k_3 - a_2^2 \\ e_2 = k_3^2 + k_4^2 - a_1^2 + 2a_2k_3 + a_2^2 \end{cases} \quad (6)$$

we have:

$$\begin{cases} \theta_1 + \theta_2 = -2\tan^{-1}((s - 2a_2k_4)/e_2) \\ \theta_1 = 2\tan^{-1}((s + 2a_1k_4)/e_1) \end{cases} . \quad (7)$$

$$\begin{cases} \theta_1 + \theta_2 = -2\tan^{-1}((-s - 2a_2k_4)/e_2) \\ \theta_1 = 2\tan^{-1}((-s + 2a_1k_4)/e_1) \end{cases}$$

In (7), two solutions for  $\theta_1$  and  $\theta_2$  can be obtained. When these two solutions are substituted into (5), two sets of  $\theta_i (i=1,2,3,4)$  are obtained. The solutions represent a continuous work space, and the infeasible solution will be rejected by considering the constraints of the joint space.

#### IV. NSGA-II-BASED TRAJECTORY PLANNING

To achieve a collision-free grasping or other manipulation tasks in practical environments, a feasible trajectory for the manipulator's motion should be planned [15]; the trajectory should not only satisfy free collision but also some other constraints and objectives. This paper utilizes the well-known optimization approach, i.e., NSGA-II, to achieve the planning because this approach is convenient and accurate in solving optimization problem even with complex constraints. Here, we assume that the UAV already moved to the grasping place and that the manipulator possesses a large redundancy in work space for grasping.

##### A. Mathematical Trajectory Formulation

As discussed previously, the proposed manipulator contains four joints and the gripper joint each driven by a servo motor. Given that the wrist joint can only rotate the end effector but not affect the position, only three DoFs will be considered for the proposed aerial manipulator. Notably, the proposed approach is also suitable for manipulators with high DoFs. The aerial manipulator joints are controlled in continuous space. Thus, the trajectories of each joint can be mathematically described by a continuous curve. The quintic curve is utilized because it exhibits continuous differential angles and velocities and continuous accelerations. The mathematic equation of the  $i$ -th joint curve is given as follows:

$$\begin{cases} \theta_i = \mathbf{c}_i^T [1 \ t \ t^2 \ t^3 \ t^4 \ t^5]^T \\ \omega_i = \mathbf{c}_i^T [0 \ 1 \ 2t \ 3t^2 \ 4t^3 \ 5t^4]^T \\ \alpha_i = \mathbf{c}_i^T [0 \ 0 \ 2 \ 6t \ 12t^2 \ 20t^3]^T \end{cases}, \quad (8)$$

where  $\mathbf{c}_i \in \mathbb{R}^5$  denotes the polynomial parameter vector,  $t$  denotes the time,  $\omega_i$  and  $\alpha_i$  denote the  $i$ -th joint angular velocity and angular acceleration respectively. When all the joints are stacked together, and the matrix form is used, the following equations are obtained:

$$\begin{cases} \Theta = \mathbf{C} [1 \ t \ t^2 \ t^3 \ t^4 \ t^5]^T \\ \Omega = \dot{\Theta} = \mathbf{C} [0 \ 1 \ 2t \ 3t^2 \ 4t^3 \ 5t^4]^T \\ \mathbf{A} = \ddot{\Theta} = \mathbf{C} [0 \ 0 \ 2 \ 6t \ 12t^2 \ 20t^3]^T \end{cases}, \quad (9)$$

where  $\mathbf{C} \in \mathbb{R}^{q \times 5}$  denotes the polynomial parameter vector;  $\Theta \in \mathbb{R}^q$ ,  $\Omega \in \mathbb{R}^q$ , and  $\mathbf{A} \in \mathbb{R}^q$  denote the joint angle, angular velocity, and angular acceleration vectors, respectively; and  $q$  denotes the number of joints involved in planning.

To ensure that the trajectory planning presents flexibility and improved computational performance, two-stage quintic curve is utilized instead of the traditional single-stage one.  $\mathbf{C}_a$  and  $\mathbf{C}_b$  denote the parameter matrix of each stage on the quintic curve.  $T_a$  and  $T_b$  denote the durations of the quintic curve stages, i.e.,  $T_a = t_e - t_m$ ,  $T_b = t_e - t_m$ , where  $t_e$  and  $t_m$  are defined as the end and intermediate times, respectively. The trajectory curve is determined distinctly with the boundary conditions shown in Table I.

TABLE I TWO-STAGE QUANTIC CURVE BOUNDARY CONDITIONS

$\Theta_s, \Omega_s$ and $\mathbf{A}_s$	Initial joint angle, angular velocity, and angular acceleration, respectively
$\Theta_m, \Omega_m$ and $\mathbf{A}_m$	Intermediate joint angle, angular velocity, and angular acceleration, respectively
$\Theta_e, \Omega_e$ and $\mathbf{A}_e$	End joint angle, angular velocity, and angular acceleration, respectively

##### B. Objectives and Constraints for Trajectory Planning

To move the end effector and grasp the object as soon as possible, we define the following objectives:

$$f_1(\mathbf{S}) = t_e, f_2(\mathbf{S}) = L_{arc}, \quad (10)$$

where  $L_{arc}$  is the trajectory length of the end effector. When  $\Delta t$  denotes the sampling time, the sampling number is obtained as follows:

$$N = t_e / \Delta t + 1. \quad (11)$$

According to the forward kinematics (3), we can calculate the end-effector position at the  $j$ -th time stamp, which is defined as  $\mathbf{V}_{pj}$ . When all the discrete pose increments are added,  $L_{arc}$  is calculated as follows:

$$L_{arc} = \sum_{j=1}^{N-1} \|\mathbf{V}_{pj} - \mathbf{V}_{pj-1}\|_2 \quad (12)$$

In addition to the objectives defined in (10), the trajectory should also satisfy several constraints during the manipulation, including the limitations of joint angles, velocity, and acceleration and the constraint of collision avoidance. The valid ranges of these mentioned constraints are considered. With regard to the constraint of joint limits,  $\Theta_j, \Omega_j$ , and  $\mathbf{A}_j$  at each sampling period are verified whether existing in the available work space. When considering joint angles  $\Theta_j$  at the  $j$ -th sampling moment, the positions of all joints are obtained through forward kinematics (3). To reduce the computational complexity, the known obstacles are simplified and discretized into point set  $\mathbf{Q}$ . The number of obstacle points in the set  $\mathbf{Q}$  is  $N_Q$ , and the joint link of the manipulator is reduced to a line segment. The shortest distance  $d_{min}$  between the  $k$ -th obstacle in set  $\mathbf{Q}$ , and the simplified line segment of the robot arm is considered. If  $d_{min}$

is smaller than a predefined safe threshold  $d_{\text{safe}}$ , then the manipulator will collide with the obstacle.

### C. NSGA-II-based Trajectory Optimization

Finally, the multiobjective optimization problem is formulated as follows:

$$\begin{aligned} \min F(\mathbf{S}) &= \{f_1(\mathbf{S}), f_2(\mathbf{S})\} \\ \text{s.t.} &\left\{ \begin{array}{l} \Theta_i \in \mathbf{S}_\Theta, i = 1, 2, 3, \dots, N_\Theta \\ \Omega_i \in \mathbf{S}_\Omega, i = 1, 2, 3, \dots, N_\Omega \\ \mathbf{A}_i \in \mathbf{S}_A, i = 1, 2, 3, \dots, N_A \\ \mathbf{Q}_j \in \mathbf{Q}, j = 1, 2, 3, \dots, N_Q \\ \Theta_{\min} < \Theta_i < \Theta_{\max}, i = 1, 2, 3, \dots, N_\Theta \\ \Omega_{\min} < \Omega_i < \Omega_{\max}, i = 1, 2, 3, \dots, N_\Omega \\ \mathbf{A}_{\min} < \mathbf{A}_i < \mathbf{A}_{\max}, i = 1, 2, 3, \dots, N_A \\ d_{\min} > d_{\text{safe}}, i = 1, 2, 3, \dots, N, k = 1, 2, 3, \dots, N_Q \\ 0 < t_a \leq t_{\max} \\ 0 < t_b \leq t_{\max} \end{array} \right. \quad (13) \end{aligned}$$

where  $\mathbf{S}_\Theta$  denotes the set of sampled joint angle vectors,  $\mathbf{S}_\Omega$  denotes the set of sampled joint angular velocity vectors, and  $\mathbf{S}_A$  denotes the set of sampled joint angular acceleration vectors.  $\Theta_{\min}$  and  $\Theta_{\max}$  depend on the servo motor specification, and  $t_{\max}$  is the limit of the execution time of each quintic curve. According to our experiments,  $t_{\max}$  is set to 5 s empirically. Other parameters are set according to the dynamics of the UAV robotic system.

Given that the system is hovering when grasping, the initial velocities  $\Omega_s$  are zero, and the joint angles  $\Theta_s$  are obtained from the servo motor sensor. The target joint angular velocities  $\Omega_e$  are also set to zero. The target joint angle  $\Theta_e$  is obtained from the target end-effector position through inverse kinematics. Thus, the parameter vector to be optimized is as follows:

$$\mathbf{S}_p = (t_a \ t_b \ \mathbf{A}_s^T \ \Theta_m^T \ \Omega_m^T \ \mathbf{A}_m^T \ \mathbf{A}_e^T), \quad (14)$$

where  $\mathbf{S}_p \in \mathbb{R}^k$ ;  $k = 5 \times N_{\text{links}} + 2$ . According to the form of the optimization model (13) and vector (14), real number coding is used in NSGA-II. NSGA-II is finally used to obtain the optimization result.

## V. KINEMATIC COMPENSATION AND VISUAL TRAJECTORY TRACKING

### A. Real-time Visual Compensation

With the trajectory planning algorithm in Section IV, the joint inputs w.r.t. time denoted as  $\mathbf{T}_e^b(t)$  can be obtained. The trajectory is designed on the basis of the target object pose  $\mathbf{T}_a^b$  with respect to body frame initially. However, the movement of the manipulator or other unstable factors, such as wind disturbance, may change the body or object pose

during the tracking process. This problem will prevent a successful grasping if no compensation is introduced.

Without loss of generality, we assume that the tracking camera can capture the object pose in real time. The UAV keeps track of where the previous  $\mathbf{T}_a^b$  is located. The trajectory planning aims to realize the collision-free target grasping. We also assume that the body in the grasping process will not generate a serious shift. Thus, we do not consider the free-collision of each joint, except for the end effector. With regard to the body frame of the Cartesian space (the operating space), the trajectory should be relative to the target object. Hence, the target is considered a reference, given that that the trajectory  $\mathbf{T}_a^e(t)$  relative to the target frame should remain the same as the planned trajectory.  $\mathbf{T}_a^b(t)$  denotes the tracked pose of target object w.r.t. the body frame. We can calculate the compensated item for the changed trajectory as follows:

$$\mathbf{T}_{er}^b(t) = \mathbf{T}_a^b(t) \begin{bmatrix} \mathbf{R}_a^{bT} & -\mathbf{R}_a^{bT} \mathbf{t}_a^b \\ \mathbf{0}_3^T & 1 \end{bmatrix} \mathbf{T}_e^b(t), \quad (15)$$

where  $\mathbf{R}_a^b$  and  $\mathbf{t}_a^b$  denote the rotation and translation parts of  $\mathbf{T}_a^b$ , respectively. Subsequently, we can obtain the compensated joint poses from  $\mathbf{T}_{er}^b(t)$  by the inverse kinematics in Section III.

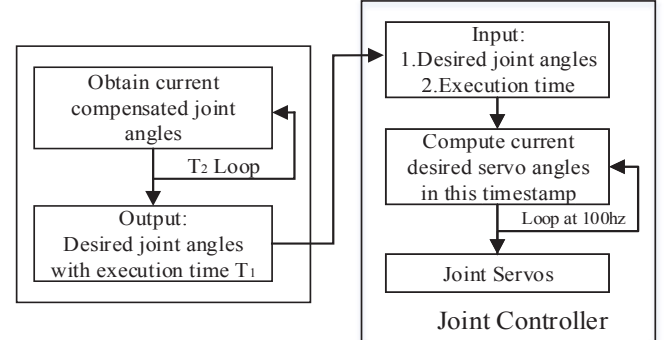


Figure 3. Flow chart of trajectory following controller by using differential frequency adjusts.

### B. Trajectory Tracking based on A Filter Controller

Many unavoidable factors inevitably exist during practical grasping task. For instance, the  $\mathbf{T}_a^b(t)$  may not be obtained in real time. Additionally, the compensated items under the joint space derived from  $\mathbf{T}_{er}^b(t)$  may be out of workspace. Given these unstable factors, an accurate trajectory following controller is difficult to achieve. We propose an effective filter controller that can address the problem. Nevertheless, the proposed method is designed on the basis of engineering experience, that is, without theoretical support. However, this method performs considerably well in our experiments. Fig. 3 shows the flow chart of the trajectory tracking controller.  $T_1$  denotes the maximum execution time for the servo motor control, and  $T_2$  denotes the sampling period of the trajectory compensation.  $T_1$  and  $T_2$  depend on the practical characters of the servo motors, and they are set as 0.2 and 0.1 s in our experiments.

## VI. EXPERIMENTS AND DISCUSSION

### A. Experimental Setup

The hardware configuration of the proposed aerial manipulator mainly contains a Pixhawk flight controller [16], a servo motor controller for the manipulator joints and grippers, and an onboard computer Intel NUC I7-5557U. The tracking camera is a low-cost CMOS module with a resolution of  $640 \times 480$  at 60 Hz. To simplify the tracking process, the well-known AprilTag [17] was attached on the target to provide a 6-DoF relative target pose. Notably, the binocular or RGBD camera can also be used to provide the 6-DoF pose information. The pose detection frequency by AprilTag reaches an average of 23 frames per second in our experiments. The motion capture system was utilized for the position feedback of UAV control. The wheelbase of the octocopter is 550 mm, the thrust capacity of the octocopter is about 8960 g, the total weight of the aerial manipulator system (including a lithium battery) is 5464 g, the weight of battery is 930 g, the weight of arm is 545 g, the weight of gripper is 26 g, and the payload weight of arm is about 200 g.

### B. Results of the NSGA-II-based Trajectory Planning

Experiments were performed to verify the performance of NSGA-II-based trajectory planning method. The parameters of NSGA-II for the experiments are presented in Table II. Fig. 4 illustrates the experimental object to be grasped. The shape of the target object can only be grasped horizontally. Thus, the trajectory planning is necessary to ensure safety grasping.

TABLE II NSGA-II PARAMETERS

Populations	60	Variance rate	0.5
Iterations	150	Crossover distribution index	50
Crossover rate	1.0	Variance distribution index	20

TABLE III OPTIMAL TRAJECTORY PLANNING RESULT

Objective 1 (s)		Objective 2 (m)		$t_a$	$t_b$
2.49136		0.229282		1.20773	1.28363
Joint	$\mathbf{A}_s$	$\Theta_m$	$\Omega_m$	$\mathbf{A}_m$	$\mathbf{A}_e$
1	-2.1723	-1.2865	0.01509	0.2072	-2.90757
2	3.11848	2.2845	-0.9824	1.3977	2.50529
3	-1.32415	0.3641	0.97405	1.0190	-0.16438

The initial and end angles of the wrist joint of the end effector are both set to zero, i.e., maintaining horizontally. The initial and end positions of the end effector are set as  $(0.25, -0.1)$  and  $(0.25, -0.22)$ . The velocity and acceleration limits for each joint are set as  $[-\pi/2, \pi/2]$ rad/s and  $[-\pi, \pi]$ rad/s<sup>2</sup>, respectively. The maximum trajectory durations are set to 5s, i.e.,  $T_a \in (0, 5]$  and  $T_b \in (0, 5]$ . Table III illustrates the solution in the Pareto front [12]. The time cost of the algorithm is approximately 1793 ms. The planned trajectory and the curves of each joint angle, velocity, and acceleration are displayed in Fig. 5. Notably, all the constraints are satisfied. According to Fig. 5(b), the object is shaken slightly, and the compensation addresses the shaking.

The final actual trajectory of the end effector is relatively smooth under the proposed filter controller.

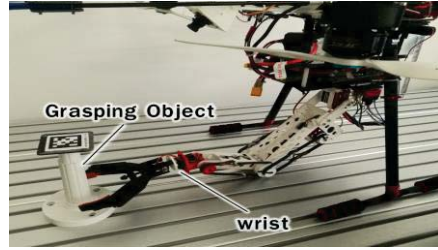


Figure 4. Experimental object to be grasped.

### C. Experimental Result of Aerial Grasping

The global positioning of the UAV is provided by a motion capture system. The grasping process is divided into two phases. The aerial manipulator first flies toward the target object by using the onboard visual tracking system. Afterward, the system performs grasping. Fig. 6 shows the snapshots of the aerial grasping. The position of the aerial manipulator and the target object are shaken with a magnitude of approximately 8 cm due to dynamic instability and wind interference. However, the grasping still achieves a good performance. The performance is clearly observed in the attached video of the experiment. Several experiments were performed by changing the UAV's hovering position, and the object was grasped successfully.

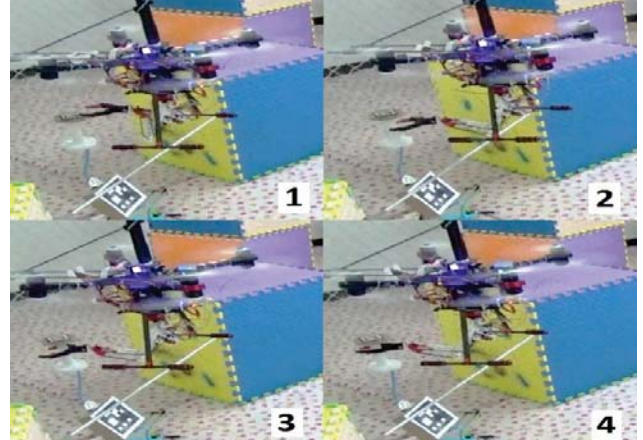


Figure 6. Snapshots of the visual compensated grasping.

## VII. CONCLUSION

This paper presents an autonomous visual grasping approach with a multi-DoF lightweight aerial manipulator. A NSGA-II-based trajectory generation method is developed to plan an optimized trajectory. The trajectory considers the kinematic model of the aerial manipulator system, and it can help in finishing the grasping task immediately and simultaneously satisfying motion constraints. The work focuses on an efficient method without the need to calibrate dynamic parameters. To obtain a successful grasping, an agile visual system combined with 1-DoF monocular camera is proposed. Furthermore, a visual compensation method with a filter controller is presented to prevent the system instability and the external interference. Finally, several experiments are performed to verify the proposed approach.

## REFERENCES

- [1] P. E. I. Pounds, D. R. Bersak and A. M. Dollar, "The yale aerial manipulator: grasping in flight," in Proc. *IEEE International Conference on Robotics and Automation*, pp. 2974-2975, 2011.
- [2] N. Michael, J. Fink and V. Kumar, "Cooperative manipulation and transportation with aerial robots," *Autonomous Robots*, vol. 30, no. 1, pp. 73-86, 2011.
- [3] A. Santamaría-Navarro, P. Grosch, V. Lippiello, J. Sola and J. Andrade-Cetto, "Uncalibrated visual servo for unmanned aerial manipulation," *IEEE/ASME Transactions on Mechatronics*, vol. 22, no. 4, pp. 1610-1621, Aug. 2017.
- [4] C. E. Doyle, *et al.*, "Avian-inspired passive perching mechanism for robotic rotorcraft," in Proc. *IEEE/RSJ International Conference on Intelligent Robots and Systems*, pp. 4975-4980, 2011.
- [5] J. Thomas, G. Loianno, K. Sreenath and V. Kumar, "Toward image based visual servoing for aerial grasping and perching," in Proc. *IEEE International Conference on Robotics and Automation*, pp. 2113-2118, 2014.
- [6] R. Mebarki, V. Lippiello and B. Siciliano, "Image-based control for dynamically cross-coupled aerial manipulation," in Proc. *IEEE/RSJ International Conference on Intelligent Robots and Systems*, pp. 4827-4833, 2014.
- [7] V. Ghadiok, J. Goldin, and W. Ren, "Autonomous indoor aerial gripping using a quadrotor," in Proc. *IEEE/RSJ International Conference on Intelligent Robots and Systems*, pp. 4645-4651, 2011.
- [8] G. Heredia *et al.*, "Control of a multirotor outdoor aerial manipulator," in Proc. *IEEE/RSJ International Conference on Intelligent Robots and Systems*, pp. 3417-3422, 2014.
- [9] G. Garimella and M. Kobilarov, "Towards model-predictive control for aerial pick-and-place," in Proc. *IEEE International Conference on Robotics and Automation*, pp. 4692-4697, 2015.
- [10] S. Kim, H. Seo, S. Choi and H. J. Kim, "Vision-guided aerial manipulation using a multirotor with a robotic arm," *IEEE/ASME Transactions on Mechatronics*, vol. 21, no. 4, pp. 1912-1923, 2016.
- [11] M. Fumagalli *et al.*, "Developing an aerial manipulator prototype: Physical interaction with the environment," *IEEE Robotics and Automation Magazine*, vol. 21, no. 3, pp. 41-50, 2014.
- [12] K. Deb, A. Pratap, S. Agarwal and T. Meyarivan, "A fast and elitist multiobjective genetic algorithm: NSGA-II," *IEEE Transactions on Evolutionary Computation*, vol. 6, no. 2, pp. 182-197, 2002.
- [13] C. D. Bellicoso, L. R. Buonocore and V. Lippiello, "Design, modeling and control of a 5-DoF light-weight robot arm for aerial manipulation," in Proc. *Mediterranean Conference on Control and Automation*, pp. 853-858, 2015.
- [14] B. Siciliano, L. Sciavicco, L. Villano and G. Oriolo, *Robotics Modeling, Planning and Control*. Springer London, 2009.
- [15] M. W. Spong, S. Hutchinson and M. Vidyasagar, *Robot modeling and control*. New York: Wiley, 2006.
- [16] L. Meier, P. Tanskanen, F. Fraundorfer and M. Pollefeys, "Pixhawk: A system for autonomous flight using onboard computer vision," in Proc. *IEEE International Conference on Robotics and Automation*, pp. 2992-2997, 2011.
- [17] E. Olson, "AprilTag: A robust and flexible visual fiducial system." in Proc. *IEEE International Conference on Robotics and Automation*, pp. 3400-3407, 2011.

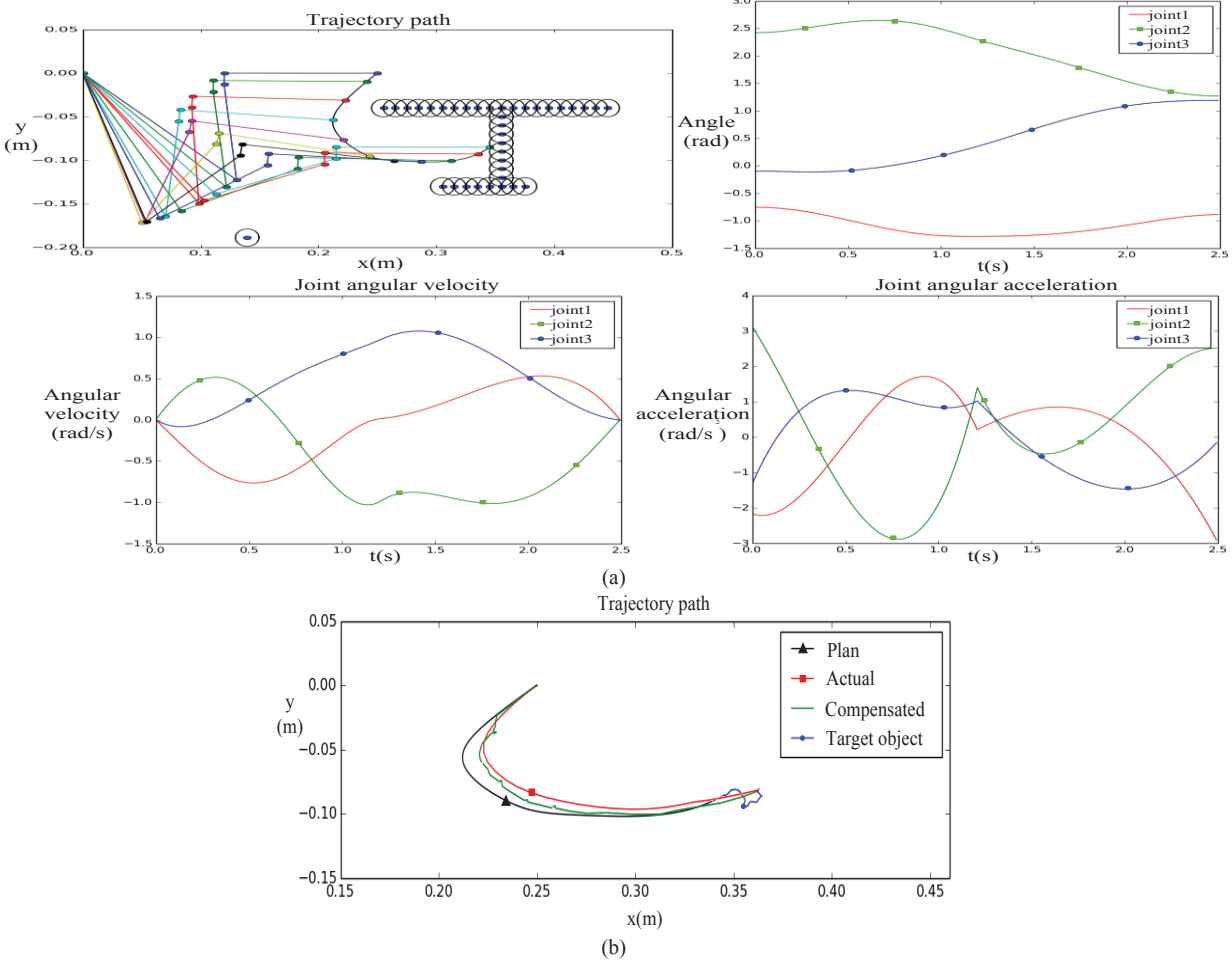


Figure 5. (a) Grasping experiment results, including the planned trajectory and the curves of the joint angles, velocities, and accelerations. (b) Comparison of the paths of the end effector, including the planned path, actual path, and compensated path. The blue curve shows the position variation of the target object w.r.t. the manipulator frame.